The nature of the proximal volcaniclastic materials from the 2021 eruption Fukutoku-Oka-no-Ba in the Izu-Bonin arc.

Kenta Yoshida*, Yoshihiko Tamura, Tomoki Sato, Erika Tanaka, Noriko Tada, Morihisa Hamada, Takeshi Hanyu, Qing Chang, Shigeaki Ono

Research Institute for Marine Geodynamics, Japan Agency for Marine-Earth Science and Technology, Natsushima-cho 2-15, Yokosuka, 237-0061 Japan.

Correspondence
Kenta Yoshida, Natsushima-cho 2-15, Yokosuka, 237-0061 Japan.
E-mail: yoshida_ken@jamstec.go.jp

Funding Information

Japan Society for the Promotion of Science, KAKENHI, Grant Nos. JP19K14825 and JP19H01999 to K.Y. and JP21H01195 to Y. T.

Conflict of interest disclosure

There are no entities or relationship, etc. presenting a potential conflict of interest requiring disclosure in relation to this manuscript.

This is a non-peer review preprint that has been submitted to *Island Arc*; future versions may have different content.

Abstract

Fukutoku-Oka-no-Ba is a submarine volcano located at 24°17.1′N/141°28.9′E in the Izu–Bonin–Mariana arc, and is one of the most active volcanoes in Japan. This volcano produced an explosive eruption in August 2021 that generated a large amount of volcaniclastic material, some of which drifted westward to Japan and the coastal area of East Asia as a pumice raft. The pumice clasts that drifted for >1000 km were mostly homogeneous and identical to those produced by past historical eruptions. The clasts have trachytic compositions (SiO_2 = 61-63 mass% and Na_2O+K_2O = 8.6-10.0 mass%) and contain augite, plagioclase, olivine (Mg# ~65), and magnetite, along with a small number of mafic enclaves containing diopside and high-Mg olivine (Mg# ~ 92).

We undertook a research cruise to investigate the proximal volcaniclastic materials by dredging. The proximal materials include pumice, weakly vesiculated lapilli, and volcanic rocks, which have trachytic composition (SiO_2 contents up to 64.5 mass%). The main minerals in the proximal material are similar to those in the drift pumice, although remnants of mafic magma do not occur in the SiO_2-rich samples. The compositional variations of the SiO_2-rich proximal samples are due to plagioclase-dominated fractional crystallization, and the higher-SiO_2 samples yielded lower temperature and pressure among the studied samples.

The petrographic and geochemical characteristics of the proximal and drift ejecta from Fukutoku-Oka-no-Ba suggest the magma reservoir was stratified into two parts. The lower part experienced magma mixing with a limited volume of mafic magma, whereas the upper part underwent plagioclase-dominated fractional crystallization. The accumulation of differentiated high-SiO_2 magma in the upper part of the magma reservoir might have increased the pressure in the magma conduit, which then exceeded the critical pressure required for an explosive eruption.

Keywords: Fukutoku-Oka-no-Ba, Izu–Bonin–Mariana arc, phreatomagmatic eruption, drift pumice

1. Introduction

A large volume of pumice clasts was generated by the 2021 eruption of Fukutoku-Oka-no-Ba (FOB) volcano, which is located at 24°17.1′N/141°28.9′E in the Izu–Bonin–Mariana arc (Fig. 1a). This is one of the most active volcanoes in Japan. The pumice clasts drifted and became distributed over a wide area around the islands of Japan and in many places in the East Asia, including Taiwan, Philippines, and Thailand (Yoshida et al., 2022a, b, c). The large amounts of drift pumice filled port areas and hindered vessel navigation, which led to significant economic losses (Maeno et al., 2022; Yoshida et al., 2022a, c; Asami and Takahashi, 2023). The drift pumice is geochemically homogeneous (Yoshida et al., 2022a) and similar to that generated during past eruptions in 1904, 1914, 1986, and 1992 (Tsuya, 1937; Yoshida et al., 1987; Kato, 1988; Nakano and Kawanabe, 1992; Sun et al., 1998), although the color and texture of the pumice are variable (Yoshida et al., 2022a). A notable characteristic of the pumice generated by FOB is the minor but common occurrence of black-colored pumice, which consists mainly of transparent brown glass with magnetite nanocrystals (i.e., nanolites) (Yoshida et al., 2022a). Although recent studies have focused on nanolite precipitation and the mechanism of large eruptions (Cáceres et al., 2020, 2021; Di Genova et al., 2020; Scarani et al., 2022), the actual processes that trigger eruptions remain unclear (Dubosq et al., 2022). The biotite-bearing hydrous mineral assemblage of nanolite and higher $Fe^{3+}/\Sigma Fe$ ratio of the nanolite-bearing glass than the nanolite-free glass indicate that oxidation due to fluid infiltration induced nanolite-precipitation and subsequent bubble nucleation, which resulted in the explosive eruption (Yoshida et al., 2023).

The 2021 eruption of FOB was large enough to be observed by satellite imaging, and the volcanic column reached a height of ~16 km, corresponding to stratospheric level (Maeno et al., 2022; Yoshida et al., 2022a). Based on Himawari-8 satellite images, Maeno et al. (2022) provided a detailed timeseries of the phreatomagmatic eruption from FOB during 13–15 August 2021. The 2021 FOB eruption column consisted of a vapor-rich plume and a small amount of volcaniclastic materials. The pumice contains virtually no hematite nanolites, which indicates that most of the pumice clasts were ejected into water and subsequently floated due to their buoyancy (Maeno et al., 2022; Yoshida et al., 2023). Whether the pumice floated or sunk depended on its microtexture (Mitchell et al., 2021), and the microtexture of the FOB pumice varies widely due to the presence of nanolites (Yoshida et al., 2022a, 2023). The drift pumice sampled on-land only represents the pumice clasts continued to float over a long transport distance (up to 4000 km). Yoshida et al. (2022b, c) noted that the pumice rafts that drifted longer distances tended to comprise smaller clasts with lesser amounts of black pumice that contained larger vesicles.

To understand the nature of the 2021 eruption and magmatic system of FOB, it is necessary to investigate the full range of erupted volcaniclastic materials, including those that did not float. As such, we undertook a research cruise using the R/V *Yokosuka* to investigate these deposits. A dredge survey was undertaken inside and outside the submarine caldera to collect fresh rock samples, both with and without significant vesiculation. In this paper, we describe the petrographic and geochemical features of these samples. These new and previously reported data constrain the nature of the magmatic system of FOB, which can be used to predict and mitigate hazards from submarine volcanoes in the far-off sea.

2. Materials and Methods

2.1. Geological Background and Research Cruise

FOB is one of the most southern volcanoes in the Izu–Bonin arc. The volcano is located within a large volcanic complex that extends approximately 15 and 30 km for E–W and N–S direction, respectively (Fig. 1b). The complex comprises the Kita-Fukutoku-Tai volcano, Kita-Fukutoku caldera, and Minami-Ioto volcano (from north to south), and FOB is the central cone of Kita-Fukutoku caldera, which is ~2 km in diameter (Ito et al., 2011). The summit of FOB before the 2021 eruption had an oval shape (elongate NE–SW) and was flat at a depth of ~30 m below sea level (Ito et al., 2011). Seismic and geomagnetic surveys indicate that a low-velocity zone exists to the north of FOB, which can be attributed to the partially molten region of the magma reservoir (Nishizawa et al., 2002; Onodera et al., 2003). The magmatic system of FOB and Kita-Fukutoku caldera are still poorly understood. Based on Nd and Pb isotopic compositions, Sun et al. (1998) suggested that the magma of FOB is distinct from those of the nearby volcanoes of Ioto, but similar to those of the Hiyoshi Volcanic Complex in the northern part of the Mariana arc.

The 2021 FOB eruption occurred in the morning of 13 August 2021 and continued to the morning of 16 August (Japan Meteorological Agency, 2021). Underwater sound and infrasound remote observations indicate that the eruption started at 5:55 AM (in Japan Standard Time; Maeno et al., 2022; Metz, 2022).

We undertook a geological survey and sampling around FOB during six dredging operations using the R/V *Yokosuka* during cruise YK22-15 from 14 to 27 August 2022. A double-towing dredging system was used (Supplementary Fig. 1). Figure 1b shows the locations of the dredging operations. Given that the cruise was carried out just 1 yr after the explosive eruption, we remained at least two nautical miles (~3.7 km) from the volcanic vent for safety reasons (green circle in Fig. 1b). We consider that the samples collected by the dredges represent the geology of the volcano, although there remains uncertainty as to whether the dredged samples are representative of their specific locations.

Three dredges (YK22-15 D03, D05, and D08) targeted the western side of the volcanic vent along the western slope of the caldera. YK22-15 D08 was a continued dredging operation of YK22-15 D03, because the D03 line was cancelled due to stacking of the dredger. YK22-15 D06 targeted the eastern slope of the outer rim of the crater and YK22-15 D07 targeted the outer slope of the topographic high from the rim of the crater. YK22-15 D04 targeted the southern slope of Kita-Fukutoku-Tai. Detailed locations of the dredges are described in the Supplementary Material.

2.2. Analytical Methods

Mineral and volcanic glass compositions were determined using a field emission gun electron microprobe (EMP) analyzer equipped with five wavelength-dispersive X-ray detectors (JEOL: JXA-8500F) at Japan Agency for Marine-Earth Science and Technology (JAMSTEC; Yokosuka, Japan). Natural and synthetic standards were used to calibrate the quantitative analyses following the procedure of Yoshida et al. (2022a). The analytical conditions were 15 kV and 10 nA for the accelerating voltage and beam current, respectively, except for analyses of olivine. For some olivine grains, we used an accelerating voltage of 20 kV and beam current of 25 nA. The beam diameter was set to 3 μm for minerals and 5 μm for glass. $Fe^{3+}/\Sigma Fe$ values for clinopyroxene were calculated such that the total cations were four on a six-oxygen basis, whereas $Fe^{3+}/\Sigma Fe$ values for magnetite were calculated for $Fe^{2+} + Mg + Mn = 1$ on a four-oxygen basis. All Fe in olivine was assumed to be ferrous. Anorthite, albite, and orthoclase contents of plagioclase were calculated as Ca/(Ca+Na+K)×100, Na/(Ca+Na+K) ×100, and K/(Ca+Na+K) ×100, respectively.

Cathodoluminescence analysis of silica minerals was conducted using a scanning electron microscope (ThermoScientific: Quanta FEG450) equipped with a cathodoluminescence system (Gatan: MonoCL 4) at JAMSTEC.

Raman spectra were obtained with a Raman spectrophotometer (RAMANtouch VIS-HP-MAST; Nanophoton) equipped with a 532 nm semiconductor green laser at JAMSTEC. The laser power on the sample surface was 1-2 mW, and data were acquired in 2 × 20 s cycles to eliminate accidental cosmic rays. The spectrometer was calibrated to the 520.7 cm^{-1} peak of a Si wafer.

Whole-rock major element compositions were determined following the methods of Tani et al. (2005) and Sato et al. (2020), by X-ray fluorescence (XRF) spectrometry (Rigaku ZSX Primus II). Prior to analysis, the samples were crushed to pebble size (5–10 mm) and desalinated using hot water (~40 °C) and by boiling in Milli-Q water. Desalinization was checked using a $AgNO_3$ solution and corresponding precipitation of AgCl, so that no precipitation occurs. The desalinized samples were then washed with Milli-Q water and acetone in an ultrasonic bath, and powdered in an agate mortar or with a Multi-beads Shocker pulverizer. Finally, a mixture of 0.4 g of sample powder and 4 g of $Li_2B_4O_7$ was fused and made into glass beads for XRF analysis. Accuracy and reproducibility of the major element data are better than ±1% and ±2 % (relative standard deviations), respectively.

We also analyzed the whole-rock trace element compositions by solution inductively coupled plasma-mass spectrometry (ICP-MS; iCAP Qc; ThermoFisher Scientific). The rock powders were digested in HF, HClO4, and HNO3. We also analyzed a reference basalt (JB-2; Jochum et al., 2016), which yielded results that are in good agreement with certified values (Table S1).

3. Results

3.1. Sample descriptions

The recovered rock samples were initially described onboard. The samples include gray to brown pumice, black volcanic rock with variable degrees of vesiculation, and tuff. For convenience, we omit the cruise number (YK22-15) and describe the dredge number with the prefix D and the sample number with the prefix R. For example, D03R01 is the first rock sample from dredge number three.

The rock samples are generally fresh and without Mn oxide coatings. The pumice clasts are mostly rounded. In contrast, the black volcanic rock samples are angular to subangular, indicating subsequent reworking was insignificant. The samples collected from the western lines (D03, D05, and D08) contain a considerable amount of pumice and angular volcanic rock clasts that are <10 cm in length (Fig. 2a-b). The most common pumice is gray in color, and is similar to those collected as drift pumice (Yoshida et al., 2022a), while some pumice is dark gray to black (Fig. 2c). Although the drift pumice contains black spots including mafic enclaves and plagioclase-dominated crystal clots with nanolite-bearing glass, such features are rare in the dredged samples. Tuff breccia clasts up to 20 cm in size were also recovered. Several black lapilli clasts with a vitreous luster (i.e., obsidian) were also found (Fig. 2d). Based on the deep-sea camera observations, the seafloor around the D08 position was calm and covered with white volcanic ash (Fig. 1c). The dredge D06 was conducted on the southeastern side of the central vent, and sampled black volcanic rocks with variable degrees of vesiculation that were up to 10 cm in size (Fig. 2e). Smaller pumice clasts were also recovered. During dredge D07 on the northeastern slope of the outer caldera rim, an outcrop of black volcanic rocks was observed by the deep-sea camera (Fig. 1d). The volcanic rock sample D07R01 has a pillow-like structure (Fig. 2f), indicative of the subaqueous extrusion. Dredge D07 also recovered large pumice clasts up to 22 cm in length, which have a well-developed tubular texture (Fig. 2g). This texture is referred to as woody pumice, and is considered to form during a submarine eruption (Kato, 1987).

Nine representative samples, including volcanic rock and pumice clasts, were selected for petrographic and geochemical investigations.

3.2. Whole Rock Geochemistry

The nine samples have trachytic compositions regardless of their appearance (i.e., glassy volcanic rock/lapilli or pumice; Table 1; Fig. 3a), with higher SiO_2 (63.7–64.4 mass% on an anhydrous basis) and total alkali (Na_2O+K_2O = 10.2–10.4 mass%) contents as compared with the drift pumice (Yoshida et al., 2022a, b), except for one sample (Fig. 3a). The glassy lapilli sample D06R02 was collected from the southeastern slope of the caldera and has a slightly SiO_2-poor composition that overlaps those of the drift pumice. The whole rock major element compositions of the dredged samples and drift pumice define linear trends in Harker diagrams (Figs. 3b–d).

Plots of SiO_2 versus selected trace elements are shown in Figures 3e–f. Three drift pumice compositions reported by Yoshida et al. (2022a) are also shown. Zr/Y and La/Sm ratios of the dredged samples are approximately 9.0 and 8.3, respectively, which are higher than those of the drift pumice, except for sample D06R02 (Figs. 3e–f) that has a similar composition as the drift pumice.

N-MORB-normalized trace element diagrams show that the studied samples have similar patterns to the drift pumice from the 1986 and 2021 eruptions (Fig. 3g)

3.3. Petrography and Mineral/Volcanic Glass Chemistry

Based on the occurrence of microlites that are visible under an optical microscope, the pumice and volcanic rock samples respectively were subdivided into microlite-rich and microlite-free types (Table 1; Figs. 4a–b). Regardless of the appearance of the pumice or volcanic rock, and occurrence of microlites, all the samples contain a similar phenocryst mineral assemblage of clinopyroxene (Cpx), plagioclase (Pl), olivine (Ol), and magnetite (Mag) (Fig. 4b), with minor amounts of apatite occurring as inclusions and a groundmass phase (Fig. 4c). In a few samples, pyrrhotite occurs as inclusions in clinopyroxene and plagioclase. The microlite-rich pumice clast D08R11 contains cristobalite (Crs) in relatively large vesicles (Figs. 4e and 5d).

The microlite-free glassy samples (D06R02 and D08R04) contain pale brown groundmass glass (Fig. 4a) that is weakly vesiculated. In contrast, the microlite-rich glassy samples (D03R01, D07R01, D07R05, and D06R01) contain dark brown groundmass glass (Fig. 4b) with abundant microlites of plagioclase and magnetite (Fig. 5a–b). Figure 4b shows that the abundance of microlites is nearly zero in the interstitial glass between the phenocryst minerals. Raman microscopy revealed that the dark brown glass in the microlite-rich samples has a Raman peak of magnetite nanolites at ~670 cm^{-1}, while this peak was not recognized for the pale brown glass in the microlite-free samples (Fig. 4f).

The microlite-free pumice sample (D03R03) is gray and has a strongly vesiculated groundmass that consists of colorless glass. The glass surrounding the plagioclase phenocrysts is colorless and nanolite-free (Fig. 4c), while the plagioclase phenocrysts in the drift pumice is commonly associated with nanolite-bearing brown glass, even though the groundmass glass is generally colorless. Figure 4d shows a plagioclase phenocryst in a gray-type drift pumice from the FOB eruption that was collected in Thailand and described by Yoshida et al. (2022b). The nanolite-rich pumice sample (D08R11) has a dusty and highly vesiculated groundmass (Fig. 4e). Although most vesicles are very small (<50 μm), we identified large vesicles (>100 μm) that occasionally contain spherical cristobalite (Fig. 4e).

Mafic magma components such as mafic enclaves and Mg-rich olivine (Mg# ~90) were not recognized in the dredged samples.

Below, we describe the characteristics of respective minerals and volcanic glass. Representative EMP analyses are shown in Tables 2–4.

Plagioclase is the most abundant minerals in the studied samples, and is generally euhedral and up to 5mm in length. Plagioclase generally has a Ca-rich core with $An_{40-49}Ab_{54-48}Or_{4-3}$ and a Ca-poor rim with $An_{30-38}Ab_{56-62}Or_{7-4}$ (Figs. 5a and 6a), which is similar to the core-rim compositions reported for the drift pumice from FOB (Yoshida et al., 2022a). Brown-colored melt inclusions are common, some of which contain optically-visible microlites of magnetite.

Clinopyroxene in the studied samples has an almost homogeneous augite composition with Mg# ~80 (Fig. 6b). Samples D06R01 and D07R05 exhibit significant zonation in Fe-Mg ratios, with D07R05 having cores with Mg# = 93 and rims with Mg# = 78, and D06R02 having cores with Mg# = 72 and rims with Mg# = 80 (Figs. 5b & 6b).

Olivine in the studied samples exhibits mostly homogeneous with Fo_{62-65}, where olivine in sample

D07R01, D07R05, and D08R11 exhibits increase in Fe contents in the outermost rims (Fig. 5c).

Magnetite in the studied samples occurs both as inclusions and a groundmass mineral. The magnetite contains considerable amounts of TiO_2 (up to 11 mass%) and Al_2O_3 (up to 3.2 mass%). The MgO content of magnetite is a useful proxy for temperature (Canil and Lacourse, 2020). The $X_{Mg\text{-}mag}$ values (Mg/[Mg + ΣFe]) vary among samples, but are mostly $X_{Mg\text{-}mag} = 0.06$ (Fig. 6c). D07R01 has the lowest $X_{Mg\text{-}mag}$ values for fine-grained magnetite in the groundmass ($X_{Mg\text{-}mag}$ = 0.044–0.048), whereas the magnetite in Ca-poor rims yielded higher $X_{Mg\text{-}mag}$ values of 0.053-0.057 (Fig. 5a). The highest $X_{Mg\text{-}mag}$ values were obtained for sample D06R02, which is a microlite-free volcanic rock, with $X_{Mg\text{-}mag}$ = 0.063–0.072.

The presence of cristobalite in sample D08R11 was confirmed by Raman spectroscopy (Fig. 5d). EMP analysis showed the impurity of Al_2O_3 and Na_2O for 1.0 and 0.6 mass%, respectively (Table 4), corresponding to similar molar amounts (~0.0115 on a two-oxygen basis; Table 4). This is indicative of the incorporation of Al and Na as $[AlO_4/Na^+]^0$ (Schipper et al., 2020). Cathodoluminescence imaging of the cristobalite clearly revealed a radial zoning, which is characteristic of chemical vapor deposition (Schipper et al., 2020). The occurrence of cristobalite in sample D08R11 is similar to that of other deep-sea cristobalite occurrences, such as rhyolite in the Havre, Kermadec Arc (Ikegami et al., 2018), and Kikai Caldera, Japan (Hamada et al., 2023).

Glass chemistry was also determined by EMP analysis. For the microlite-rich samples, the sites of EMP analyses were carefully determined using backscattered electron images and the results showing the mineral signature were rejected as mixtures. The glass in the dredged samples has relatively high SiO_2 (>65 mass%) and total alkali (Na_2O+K_2O > 10 mass%) contents. The glassy lapilli sample (D06R02), with a whole-rock composition similar to those of the previously reported drift pumice data (Fig. 6d) also has a similar glass composition as the drift pumice (Maeno et al., 2022; Yoshida et al., 2022a). The microlite-rich pumice sample (D08R11) has a wide range of SiO_2 contents (64–73 mass%) and exhibits a negative correlation between SiO_2 and $Na_2O + K_2O$ (Fig. 6d). The glass compositions for each sample vary with the whole-rock compositions except for sample D08R11. For example, D07R01 and D07R05 have the most SiO_2-rich compositions (Fig. 6e). We did not find melt inclusions with low SiO_2 contents (<60 mass%) like those reported from the drift pumice.

The groundmass glass in sample D08R11 is heterogeneous with respect to halogen contents, and has a lower Cl content (<0.2 mass%) as compared with the other samples (0.3–0.4 mass%; Fig. 6e). The groundmass glass of the eastern dredge samples (D07R01, D07R05, and D06R01) has relatively higher Cl contents (up to 0.4 mass%), whereas samples from the western dredges and sample D06R02 have Cl contents of ~0.3 mass%.

4. *P*–*T* Estimates

Since pressure estimation using the available mineral paragenesis is not easy, Yoshida et al. (2022a) used a machine-learning-based clinopyroxene single mineral geobarometer (Petrelli et al., 2020) for the drift pumice from FOB, and obtained a pressure of ~250 MPa for the magma reservoir. In the present study, we also used the same clinopyroxene geobarometer (Table 3). Most samples consistently yielded pressures range of 215–279 MPa, except for two samples that yielded higher (D03R01 = 388 MPa) and lower (D07R01 = 177 MPa) pressures. The cores of zoned clinopyroxene in samples D07R05 and D06R01 yielded higher pressures of 445 and 371 MPa, respectively.

Another pressure indicator is the Cl content of groundmass glass. Figure 6e shows that the western samples (D03R01, D03R03, and D08R04) and sample D06R02 have Cl contents of ~0.3 mass%, whereas the eastern samples (D07R01, D07R05, and D06R01) have Cl contents of up to 0.4 mass%. The glass in sample D08R11 has very low Cl contents down to mostly zero. Based on the experimental studies, the maximum Cl solubility in alkaline melts, such as trachyte, exhibits a negative correlation with increasing pressure and is mostly independent of for compositional differences (Signorelli and Carroll, 2002; Balcone-Boissard et al., 2016). A Cl content of 0.4 mass% corresponds to a pressure of <200 MPa, and thus the higher Cl contents of the eastern samples (except for D06R02) can indicate a lower pressure of their equilibration.

Temperature conditions can be determined using the magnetite geothermometer (Canil and Lacourse, 2020) where $X_{\text{Mg-mag}}$ values can be transformed into temperatures. As shown in Figure 6c, the calculated temperatures for most samples are 920–940 °C, where sample D06R02 yielded higher temperatures of 940–960 °C. Rim compositions of the groundmass magnetite in some samples (D08R11, D07R01, F07R05, and F06R01) yielded temperatures of <900 °C (Fig. 6c). All of these low-temperature samples contain abundant microlites in the groundmass. In sample D07R01, magnetite inclusions in the plagioclase rims yielded $X_{\text{Mg-mag}} \sim 0.06$, corresponding to a temperature of ~925 °C whereas those in the groundmass yielded temperatures of 882–896 °C.

Other conventional geothermometers were applied to mineral-melt pairs carefully selected after thinsection observations. The olivine-melt geothermometer (Putirka et al., 2007) was applied to a melt inclusion and surrounding olivine in sample D07R05 and yielded a temperature of 940 °C. The olivine-melt pair in sample D03R01 yielded a higher temperature of 962 °C. The clinopyroxene-melt geothermometer (Neave and Putirka, 2017) was applied to a melt inclusion-clinopyroxene pair in sample D03R01 and yielded a temperature of 981 °C and pressure of 90 MPa. According to Perkins and Vielzeuf (1992), olivine and clinopyroxene compositions can exist in equilibrium, and thus olivine-melt and clinopyroxene-melt pairs might reflect similar conditions in the magma reservoir, although the pressure value obtained from clinopyroxene-melt pair (D03R01) is apparently lower than other estimates. The plagioclase-melt geothermometer (Putirka, 2008) was applied to the plagioclase rims ($An_{31}Ab_{61}Or_8$) and groundmass glass in sample D07D01, and yielded a temperature of 908–964 °C under the assumption of 0–2 mass % of H_2O in melt.

In summary, the coarse-grained phenocryst minerals consistently yielded temperatures of 920–980 °C, whereas rims of coarse-grained magnetite and fine-grained magnetite recorded lower temperatures down to 882 °C.

5. Discussion

5.1. The variation of magma composition

Bivariate compositional diagrams of the major elements (Figs. 3b–d) show we linear trends in the low- and high-SiO_2 ranges (61.0–63.5 and 63.5–64.5 mass%, respectively). The reported whole-rock compositions of the drift pumice, including past eruptions, are variable and scattered (Fig. 3a), and plot in the low-SiO_2 range. Selected trace element ratios also exhibit differences between low- and high-SiO_2 samples (Fig. 3e-f). We also show the trace element composition of mafic melt inclusions found in olivine and clinopyroxene (Yoshida et al., 2022a). In the magmatic system of FOB, remnants of primitive mafic magma are limitedly recognized, and include mafic melt inclusions (Maeno et al., 2022; Yoshida et al., 2022a), high-Mg olivine (Kato, 1988; Yoshida et al., 2022a, b), and calcic plagioclase (Yoshida et al., 2022a), most of which occur within or are closely associated with black pumice (Yoshida et al., 2022a, b). The lower Zr/Y and La/Sm ratios of the drift pumice (i.e., low-SiO_2 range) as compared with the dredged samples (i.e., high-SiO_2 range) can be explained by the effect of the mafic melt component, although the whole-rock compositions show little change. Relatively scattered compositions in the low-SiO_2 range (Fig. 3a) could reflect heterogeneity in the magma reservoir caused by partial mixing with a small amount of mafic component.

In contrast, the compositional trends in the higher-SiO_2 range are characterized by moderate changes in all elements and a CaO decrease with increase in SiO_2. We modeled the compositional change from the medium-SiO_2 sample (D08R04) to the highest-SiO_2 sample (D07R05) by assuming fractional crystallization of the minerals in sample D08R04 (Tables 2-4). As a result, the difference between samples D08R04 and D07R05 can be best explained by extraction of 5.6% plagioclase, 0.3% clinopyroxene, 0.2% olivine, and 0.5% magnetite (i.e., fractionation path A in Figs. 3b–d).

The model calculations indicate that the FOB magma compositions reflect the occurrence of mixing and fractionating domains. The former domain is characterized by low-SiO_2 compositions partly due to the involvement of a small amount of mafic magma. This domain is heterogeneous which may be due to incomplete mixing. In contrast, the SiO_2-rich samples represent a gradual change due to plagioclase-dominated fractionation. The SiO_2-rich samples contain high-Cl glass (Fig. 6f), which is an indicative of low pressure, and this fractionating domain might represent the upper most part of the magma reservoir that is not mixing with the deeper part of the reservoir.

5.2. Implications for the FOB Magmatic System

We undertook dredge sampling around the area of FOB, including the outer slope of Kita-Fukutoku caldera (Fig. 1b). Although previous studies reported the drift pumice had a trachytic composition with SiO_2 <~63 mass%, our dredged samples included more SiO_2-rich samples with SiO_2 > 64 mass%. Both the SiO_2-rich and -poor samples have high total alkali contents of up to 10.5 mass%, and thus we consider that all these samples represent the magma reservoir of FOB.

The crustal structure beneath FOB was investigated by acoustic and geomagnetic surveys of Nishizawa et al. (2002) and Onodera et al. (2003). The geomagnetic data indicate a low geomagnetic anomaly in the northwestern region of the volcanic vent of FOB. Onodera et al. (2003) interpreted this anomaly to represent partially molten rocks (i.e., the magma reservoir).

The dredge D07 was conducted on the outer slope of Kita-Fukutoku caldera and volcanic rock samples were collected from a seafloor outcrop (Fig. 1d). Although it is unclear whether these samples were generated by the recent volcanic activity of FOB or represent an older volcanic unit of Kita-Fukutoku caldera, a consistent trend including volcaniclastic materials collected from the inside of the caldera indicates that the chemical composition of the D07 samples reflects the endmember characteristics of the current FOB magma reservoir. The samples from D07 have the most SiO_2-rich compositions and lowest temperatures of ~880 °C (Fig. 6c), which can be interpreted to reflect plagioclase-dominated fractional crystallization during cooling.

The pumice sample containing cristobalite (D08R11) possibly represents remnant volcaniclastic material deposited within the conduit, which was ejected during the early stage of the eruption. Cristobalite occurring in vacancies in volcanic rocks are common in submarine volcanoes (e.g., Ikegami et al., 2018; Hamada et al., 2023), as well as in on-land volcanoes (e.g., Schipper et al., 2017). Schipper et al. (2017, 2020) suggested that cristobalite crystallizes by chemical vapor deposition due to the degassing of halogen species (HF and HCl), and provides evidence of shallow and slow cooling typical of a volcanic plug. After the 2021 eruption, FOB exhibited weak degassing activity, which is evident from the bubbles reaching the sea surface above the summit (Fig. 7a). Samples such as D08R11 could have been generated during inter-eruption activity in a blocked volcanic vent.

Consequently, our results for the dredged samples can be summarized as follows (Fig. 7b). The magma reservoir of FOB is heterogeneous and consists of two domains. Most of the volcaniclastic materials ejected by the 2021 FOB eruption (i.e., pumice) were derived from the deeper low-SiO_2 domain. The deeper domain is characterized by the involvement of a small amount of mafic magma, as is evident from some trace elements (Figs. 3e–f), and the limited occurrence of mafic enclaves (Yoshida et al., 2022a) and nanolite-bearing black pumice (Yoshida et al., 2023). Based on the micro- to nano-scale petrographical observation, Yoshida et al. (2023) suggested that the intrusion of hydrous mafic magma induced oxidation and corresponding nanolite-precipitation in the limited volume of the magma which enhanced heterogeneous bubble nucleation (Pistone et al., 2017; Di Genova et al., 2020). This bubble nucleation served magma convection in the deeper domain, resulting in incomplete mixing and considerable heterogeneity. The shallower part is characterized by higher-SiO_2 contents and lower pressures of <200 MPa, corresponding to a depth of <8 km assuming a crustal density of 2400 kg/m^3. The shallower domain consists of more differentiated magma, indicating the gravity differentiation. The SiO_2-rich less-dense magma may have avoided magma convection and mixing with the deeper domain and does not contain mafic magma components. As a result, the whole-rock and melt compositions became more SiO_2 rich, and plagioclase became more stable at lower temperatures. This SiO_2-rich magma was either ejected with the pumice and sunk immediately after the explosive eruption, or was effusively erupted from a location other than central vent of FOB, such as dredge site D07. The storage of the differentiated high-SiO_2 magma in the upper part of the magma reservoir might have plugged the volcanic conduit and increased the pressure, which ultimately led to the high explosivity of the 2021 eruption.

Summary

Proximal samples of volcaniclastic sediments and volcanic rocks of FOB exhibit differences as compared with drift pumice collected from coastal areas of Japan (i.e., >1000 km from the volcano). The proximal rocks include pumice and volcanic rocks, most of which have higher SiO_2 contents (>63.5 mass%) as compared with drift pumice from the 2021 and earlier eruptions (61–63 mass%), although the constituent minerals are the same. Compositional variations of the SiO_2-rich proximal samples resulted from plagioclase-dominated fractional crystallization, and the higher-SiO_2 samples yielded lower temperatures and pressures. The petrographic and chemical characteristics of the proximal and drifted ejecta from FOB suggest the magma reservoir contains two distinct domains.

Supplementary Materials

The detailed positions of the dredges, reference standard analysis for the whole-rock trace element composition, and the outline of the dredge procedure are provided in the Supplementary Material.

Acknowledgements

This research was partly supported by JSPS KAKENHI (grant nos. JP19K14825 and JP19H01999 to K.Y. and JP21H01195 to Y.T.), the Joint Usage and Research Program of the Earthquake Research Institute, the University of Tokyo (ERI JURP 2021-B-01). This paper also benefited from constructive reviews by XX and editorial handling by XX.

We thank Captain Y. Nakamura and the crews of the R/V *Yokosuka* and T. Sugihara at JAMSTEC for their help during cruise YK22-15. K. Noguchi and R. Fukuda at HEXaMedia are thanked for operating the unmanned aerial vehicle during the cruise.

References

Asami, M. & Takahashi, C. (2023) Drift prediction of pyroclasts released through the volcanic activity of Fukutoku-Okanoba into the marine environment. Marine Pollution Bulletin, 186, 114402.

Balcone-Boissard, H., Boudon, G., Cioni, R., Webster, J.D., Zdanowicz, G., Orsi, G., Civetta, L. (2016) Chlorine as a geobarometer for alkaline magmas: Evidence from a systematic study of the eruptions of Mount Somma-Vesvius. Scientific Reports, 6:21726

Canil, D. & Lacourse, T. (2020) Geothermometry using minor and trace elements in igneous and hydrothermal magnetite. Chemical Geology, 541, 119576.

Cáceres, F., Wadsworth, F.B., Scheu, B., Colombier, M., Madonna, C., Cimarelli, C., Hess, K.-U., Kaliwoda, M., Ruthensteiner, B., & Dingwell, D.B. (2020) Can nanolites enhance eruption explosivity? Geology, 48, 997-1001.

Cáceres, F., Scheu, B., Hess, K.-U., Cimarelli, C., Vasseur, J., Kaliwoda, M., Dingwell, D.B. (2021) From melt to crystals: The effects of cooling on Fe–Ti oxide nanolites crystallization and melt polymerization at oxidizing conditions. Chemical Geology, 563, 120057.

Di Genova, D., Brooker, R.A., Mader, H.M., Drewitt, J.W.E., Longo, A., Deubener, J., Neuvillem D.R., Fanara, S., Shebanova, O., Anzellini, S., Arzilli, F., Bamber, E.C., Hennet, L., La Spina, G., Miyajima, N. (2020) In situ observation of nanolite growth in volcanic melt: A driving force for exprosive eruptions. Science Advances, 6, eabb0413.

Dubosq, R., Schneider, D.A., Zhou, X., Gault, B., Langelier, B., Pleše, P. (2022) Bubbles and atom clusters in rock melts: A chicken and egg problem. Journal of Volcanology and Geothermal Research, 428, 107574.

Hamada, M., Hanyu, T., McIntosh, I.M., Tejada, M.L.G., Chang, Q., Kaneko, K., Kimura, J-I., Kiyosugi, K., Miyazaki, T., Nakaoka, R., Nishimura, K., Sato, T., Seama, N., Suzuki-Kamata, K., Tanaka, S., Tatsumi, Y., Ueki, K., Vaglarov, B.S., Yoshida, K. (2023) Evolution of magma supply system beneath a submarine lava dome after the 7.3-ka caldera-forming Kikai-Akahoya eruption. Journal of Volcanology and Geothermal Research, 107738. https://doi.org/10.1016/j.jvolgeores.2022.107738

Ikegami, F., McPhie, J., Carey, R., Mundana, R., Soule, A., Jutzeler, M. (2018) The eruption of submarine rhyolite lavas and domes in the deep ocean – Havre 2012, Kermadec Arc. Frontiers in Earth Science, 6: 147.

Ito, K., Kato, S., Takahashi, M., Saito, A. (2011) Volcanic topography of Fukutoku-Oka-no-ba volcano in Izu-Ogasawara arc after 2010 eruption. Report of Hydrographic and Oceanographic Researches, 47, 9-13.

Japan Meteorological Agency (2021) Monthly volcanic activity reports of Fukutoku-oka-no-ba, 2021 August. https://www.data.jma.go.jp/svd/vois/data/tokyo/STOCK/monthly_v-act_doc/tokyo/21m08/331_21m08.pdf (Webpage title was translated by the authors)

Jochum, K.P., Weis, U., Schwager, B., Stoll, B., Wilson, S.A., Haug, G.H., Andreae, M.O., Enzweiler, J. (2016) Reference values following ISO guidelines for frequently requested rock reference materials. Geostandards and Geoanalytical Research, 40, 333-350.

Kato, Y. (1987) Woody pumice generated with submarine eruption. Journal of the Geological Society of Japan, 93, 11-20.

Kato, Y. (1988) Gray pumice drifted from Fukutoku-oka-no-ba to Ryukyu Islands. Bulletin of the Volcanological Society of Japan Series 2, 33, 21-30 (in Japanese).

Lafuente B, Downs R T, Yang H, Stone N (2015) The power of databases: the RRUFF project. In: Highlights in Mineralogical Crystallography, T Armbruster and R M Danisi, eds. Berlin, Germany, W. De Gruyter, pp 1-30

Metz, D. (2022) Analysis of International Monitoring System hydrophone triplet data: Identifying the August 2021 eruption at Fukutoku-Okanoba, 24.3°N Bonin Arc. Acoustical Science and Technology, 43, 125-128.

Mitchell, S.J., Fauria, K., Houghton, B.F., & Carey, R.J. (2021) Sink or float; microtextural controls on the fate of pumice deposition during the 2012 submarine Harve eruption. Bulletin of Volcanology, 83, 80.

Nakano, S. & Kawanabe, Y. (1992) Pumices drifted to Iriomote Island in 1991. Bulletin of the Volcanological Society of Japan, 37, 95-98 (in Japanese).

Neave, D.A., & Putirka, K.D. (2017). A new clinopyroxene-liquid barometer, and implications for magma storage pressures under Icelandic rift zones. American Mineralogist, 102, 777-794.

Nishizawa, A., Ono, T., Sakamoto, H., Matsumoto, Y., Otani, Y. (2002) Ocean bottom seismographic observation at Fukutoku-okanoba submarine volcano. Report of Hydrographic Researches, 38, 101-123.

Onodera, K., Kato, T., Seo, N. (2003) Crustal structure in the vicinities of Fukutoku-okanoba submarine volcano estimated from gravity and magnetic anomalies. Report of Hydrographic and Oceanographic Researches, 39, 23-31.

Perkins, D. & Vielzeuf, D. (1977) Experimental investigation of Fe-Mg distribution between olivine and clinopyroxene: Implications for mixing properties of Fe-Mg in clinopyroxene and garnet-clinopyroxene thermometry. American Mineralogist, 77, 774-783.

Petrelli, M., Caricchi, L., & Perugini, D. (2020) Machine learning thermo-barometry: Application to clinopyroxene-bearing magmas. Journal of Geophysical Research: Solid Earth, 125, e2020JB020130.

Pistone, M., Blundy, J., Brooker, R.A., & EIMF (2017) Water transfer during magma mixing events: Insights into crystal mush rejuvenation and melt extraction process. American Mineralogist, 102, 766-776.

Putirka, K.D., Perfit, M., Ryerson, F.J., & Jackson, M.G. (2007). Ambient and excess mantle temperatures, olivine thermometry, and active vs. passive upwelling. Chemical Geology, 241, 177-206.

Putirka, K.D. (2008). Thermometers and barometers for volcanic systems. Reviews in mineralogy and geochemistry, 69, 61-120.

Sato, T., Miyazaki, T., Tamura, Y., Gill, J.B., Jutzeler, M., Senda, R., & Kimura, J.-I. The earliest stage of Izu rear-arc volcanism revealed by drilling at Site U1437, International Ocean Discovery Program Expedition 350. Island Arc, 2020, e12340

Scarani, A., Zandoná, A., Di Fiore, F., Valdivia, P., Putra, R., Miyajima, N., Bornhöft, H., Vona, A., Deubener, J., Romano, C., & Di Genova, D. (2022) A chemical threshold controls nanocrystallization and degassing behavior in basalt magmas. Communications Earth & Environment, 3: 284.

Schipper, C.I., Mandon, C., Maksimenko, A., Castro, J.M., Conway, C.E., Hauer, P., Kirilova, M., & Kilgour, G. (2017) Vapor-phase cristobalite as a durable indicator of magmatic pore structure and halogen degassing: an example from White Island volcano (New Zealand). Bulletin of Volcanology, 79, 74.

Schipper, C.I., Rickard, W.D.A., Reddy, S.M., Saxey, D.W., Castro, J.M., Fougerouse, D., Quadir, Z., Conway, C., Prior, D.J., and Lilly, K. (2020) Volcanic SiO_2-cristobalite: A natural product of chemical vapor deposition. American Mineralogist, 105, 510–524.

Signorelli, S. & Carroll, M.R. (2002) Experimental study of Cl solubility in hydrous alkaline melts: constraints on the theoretical maximum amount of Cl in trachytic and phonolitic melts. Contributions to Mineralogy and Petrology, 143, 209-218.

Sun, C.-H. Stern, R., Yoshida, T., & Kimura, J.-I. (1998) Fukutoku-oka-no-ba Volcano: A new perspective on the Alkalic Volcano Province in the Izu-Bonin-Mariana arc. The Island Arc, 7, 432-442.

Sun, W. & McDonough, W.F. (1989) Chemical and isotopic systematics of oceanic basalts: Implications for mantle composition and processes. Geological Society London Special Publications, 42, 313-345.

Tani, K., Kawabata, H., Chang, Q., Sato, K., & Tatsumi, Y. (2005) Quantitative analyses of silicate rock major and trace elements by X-ray fluorescence spectrometer: Evaluation of analytical precision and sample preparation. Frontier Research on Earth Evolution: IFREE Report for 2003-2004 vol. 2.

Tsuya, H. (1937) On the volcanics of the Huzi Volcanic zone, with special reference to the geology and petrology of the Idu and Southern Islands. Bulletin of Earthquake Research Institute, 15, 215-357.

Yoshida, K., Tamura, Y., Sato, T., Hanyu, T., Usui, Y., Chang, Q., & Ono, S. (2022a) Variety of the drift pumice clasts from the 2021 Fukutoku-Oka-no-Ba eruption, Japan. Island Arc, 31, e12441.

Yoshida, K., Tamura, Y., Sato, T., Sangmanee, C., Puttapreecha, R., & Ono, S. (2022b) Petrographic characteristics in the pumice clast deposited along the Gulf of Thailand, drifted from Fukutoku-Oka-no-Ba. Geochemical Journal, 56(5), 134-137.

Yoshida, K., Maruya, Y., & Kuwatani, T. (2022c) Chocolate-chip cookie-like pumice from the 2021 Fukutoku-Oka-no-Ba eruption: views from SNS-related geology. Japanese Magazine of Mineralogical and Petrological Sciences, 51, 220412. (in Japanese with English abstract)

Yoshida, K., Miyake, A., Okumura, S.H., Ishibashi, H., Okumura, S., Okamoto, A., Niwa, Y., Kimura, M., Sato, T., Tamura, Y., & Ono, S. (2023) Oxidation-induced nanolite crystallization triggered the 2021 phreatomagmatic eruption of Fukutoku-Oka-no-Ba, Japan. https://doi.org/10.21203/rs.3.rs-2403668/v1

Yoshida, T., Fujiwara, S., & Aoki, K. (1987) Geochemistry of Fukutoku-oka-no-ba submarine volcano, Izu-Ogasawara arc. Research Report of Laboratory of Nuclear Science, Tohoku University, 20, 202-215 (in Japanese).

Figure Captions

Figure 1. (a-b) Bathymetric maps. (a) Wide-area map showing the distribution of the Izu-Bonin arc. Bathymetric data are from ETOPO1 (doi:10.7289/V5C8276M). (b) Close-up map around FOB that shows the locations of the dredge sites. Bathymetric data were collected during the YK22-15 cruise. The green circle indicates the two-nautical-mile area of prohibited entry due to safety reasons. (c) Sandy seafloor covered with volcanic ash, which was observed during dredge D08 on the western slope of FOB. (d) Outcrop of volcanic rock observed during dredge D07 on the northeastern outer slope of Kita-Fukutoku Caldera.

Figure 2. Photographs of representative hand specimens collected during the cruise. (a) Well-vesiculated pumice, (b) black-colored lapilli, and (c) black-colored pumice collected during dredges D03 and D08 on the western slope of FOB. (d) Lapilli clasts collected during dredge D05 on the northwest of FOB. (e) Weakly vesiculated trachyte clast collected from the southeastern slope of FOB. The white areas are mainly plagioclase. (f) Volcanic rock and (g) well-developed woody pumice collected during dredge D07 on the northeastern outer slope of Kita-Fukutoku caldera.

Figure 3. (a) Total alkalis versus silica diagram showing the compositions of the dredged samples and literature data. (b-d) Plots of major elements versus SiO_2, which exhibit linear relationships. (e-f) Plots of selected trace element ratios versus SiO_2. Data for pumice from previous eruptions and melt inclusion in the 2021 drift pumice are also shown. (g) Trace element patterns of dredged samples and drift pumice from the 2021 and 1986 eruptions. Compositions were normalized to N-MORB (Sun & McDonough, 1989). Abbreviations: Y22a, Yoshida et al. (2022a); Y22b, Yoshida et al. (2022b); M22, Maeno et al. (2022); K88, Kato (1988); S98, Sun et al. (1998); Y87, Yoshida et al. (1987).

Figure 4. (a) Photomicrograph of the microlite-free lapilli clast D08R04. The groundmass consists of weakly vesiculated pale brown glass. (b) Microlite-rich lava D07R01 containing magnetite nanolites in the groundmass glass, which was confirmed by Raman spectroscopy. The interstitial glass is generally microlite-free. (c) Cross-polarized light (XPL) and plane-polarized light (PPL) photomicrographs of the pumice clast D03R03 collected from the western slope of FOB. The glass adjacent to the plagioclase phenocryst is colorless and transparent. (d) Photomicrograph of a pumice clast that drifted from FOB to the Gulf of Thailand. The groundmass surrounding the plagioclase phenocryst has a brown color, which is due to magnetite nanolite crystallization. A

detailed petrographic description was provided by Yoshida et al. (2022b). (e) Photomicrograph of the weakly vesiculated pumice clast D08R11 that contains phenocrysts of olivine, plagioclase, and magnetite. Spherical cristobalite also occurs in the vesicles. (f) Representative Raman spectra of the colored glass. Although the groundmass glass in D06R02 and D08R04 is pale brown, it does not exhibit a magnetite nanolite peak at 670 cm^{-1}. The brown glass in D07R01 exhibits a nanolite peak in its Raman spectrum.

Figure 5. (a) Backscattered electron (BSE) image of the plagioclase phenocryst in the microlite-rich volcanic rock clast D07R01. The temperatures calculated based on the $X_{Mg\text{-}mag}$ values of magnetite crystals included in the plagioclase rim are also shown. (b) Zoned clinopyroxene in the microlite-rich volcanic rock clast D07R05. The Mg# value of clinopyroxene in the core and rim, and temperatures calculated from magnetite are also shown. (c) Zoned olivine observed in sample D07R01. Representative Mg# values of the core and rim are also shown. (d) Raman spectrum of cristobalite in sample D08R11. A reference spectrum taken from the RRUFF database (Lafuente et al., 2016) is shown for comparison. (e) BSE image of the microlite-rich pumice clast D08R11, showing a mineral aggregate of plagioclase, clinopyroxene, and magnetite. Temperatures calculated for magnetite are also shown. (f) Cathodoluminescence image of the cristobalite in the boxed area of (e), which has a radial texture.

Figure 6. (a-b) Ternary compositional diagram for (a) plagioclase and (b) clinopyroxene in the studied samples. (c) $X_{Mg\text{-}mag}$ values of magnetite in the studied samples and the corresponding temperatures calculated following the method of Canil and Lacourse (2020). (d-f) Glass compositions of the studied samples shown in plots of (d) SiO_2-total alkalis, (e) SiO_2-CaO, and (f) halogen contents.

Figure 7. (a) Photographs of the sea surface above the volcanic vent of FOB taken on 22 August 2022. Floating bubbles were observed. Under the sea surface, the wall of the volcanic vent is visible. (b) Schematic diagram of the FOB magmatic system inferred from results of this study. See the main text for details.

Tables

Table 1. Whole-rock geochemical compositions of the dredged samples, showing the trace element compositions of selected samples.

Table 2. Representative compositions of plagioclase.

Footnote: *Total iron as FeO.

Table 3. Representative compositions of clinopyroxene and olivine.

Footnote: *Total iron as FeO. †Pressures for clinopyroxene were calculated using the method of on Petrelli et al. (2020).

Table 4. Representative compositions of magnetite and silica mineral.

Footnote: *Total iron as FeO. †$X_{Mg\text{-}mag}$ calculated based on Canil and Lacourse (2020) and ‡Temperature calculated using $X_{Mg\text{-}mag}$.

Fig. 1

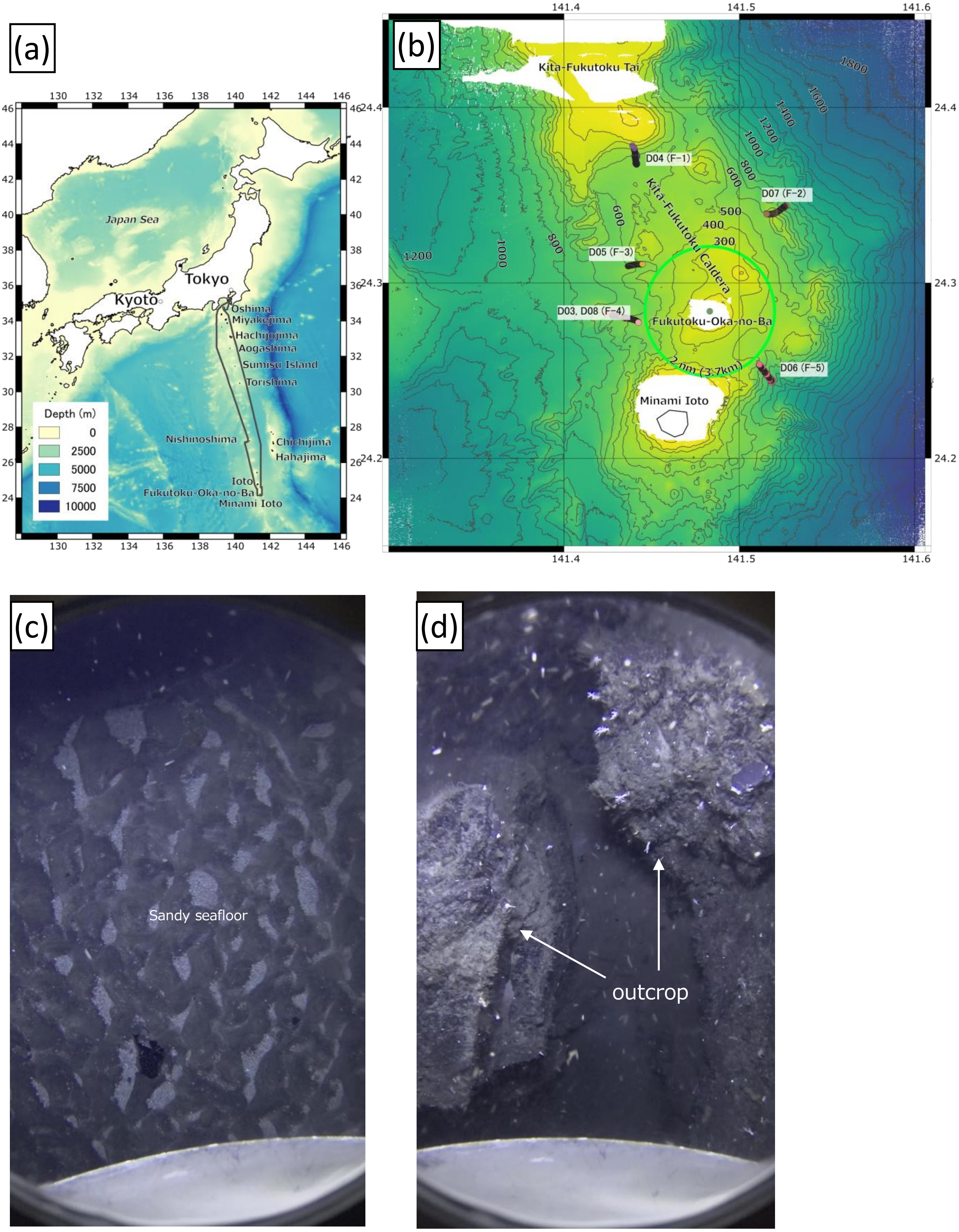
(a)
Japan Sea
Tokyo
Kyoto
Oshima
Miyakejima
Hachijojima
Aogashima
Sumisu Island
Torishima
Nishinoshima
Chichijima
Hahajima
Ioto
Fukutoku-Oka-no-Ba
Minami Ioto
Depth (m)
0
2500
5000
7500
10000
130 132 134 136 138 140 142 144 146
24 26 28 30 32 34 36 38 40 42 44 46
(b)
141.4
141.5
141.6
24.2
24.3
24.4
Kita-Fukutoku Tai
D04 (F-1)
D07 (F-2)
D05 (F-3)
D03, D08 (F-4)
D06 (F-5)
Kita-Fukutoku Caldera
Fukutoku-Oka-no-Ba
2 nm (3.7km)
Minami Ioto
300
400
500
600
800
1000
1200
1400
1600
1800
(c)
Sandy seafloor
(d)
outcrop

Fig. 2


(a)
YK22-15 D03 R03
10cm
(b)
YK22-15 D08 R04
10cm
(c)
YK22-15 D08R11
10cm
(d)
YK22-15 D05 OBS
10cm
(e)
YK22-15 D06 R01
10cm
(f)
YK22-15 D07 R01
10cm
(g)
YK22-15 D07 R08
10cm

Fig. 3

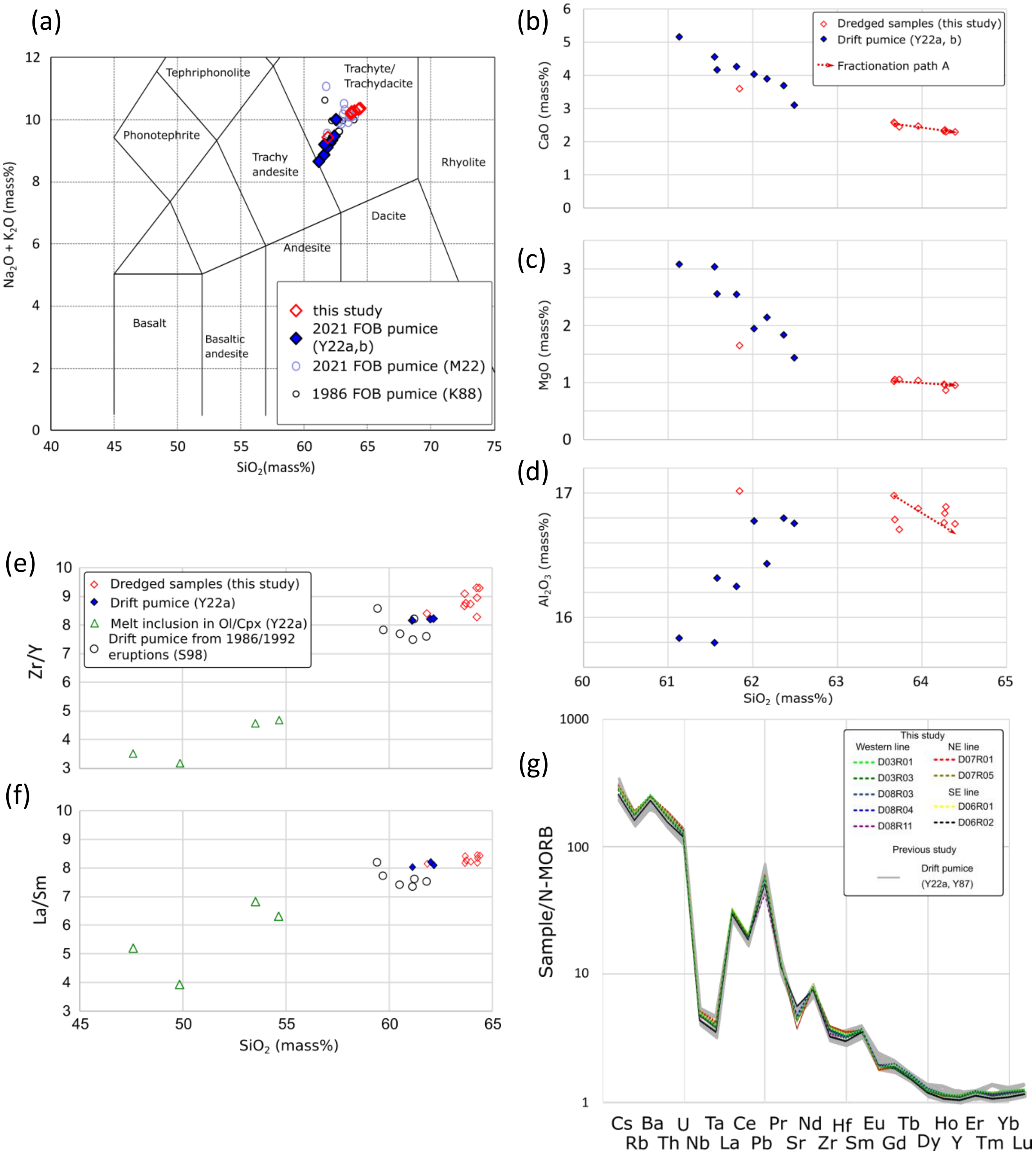

(a)
Tephriphonolite
Trachyte/
Trachydacite
Phonotephrite
Trachy
andesite
Rhyolite
Dacite
Andesite
Basalt
Basaltic
andesite
this study
2021 FOB pumice
(Y22a,b)
2021 FOB pumice (M22)
1986 FOB pumice (K88)
$Na_2O + K_2O$ (mass%)
SiO_2(mass%)
12
10
8
6
4
2
0
40
45
50
55
60
65
70
75
(b)
CaO (mass%)
6
5
4
3
2
1
0
Dredged samples (this study)
Drift pumice (Y22a, b)
Fractionation path A
(c)
MgO (mass%)
3
2
1
0
(d)
Al_2O_3 (mass%)
17
16
60
61
62
63
64
65
SiO_2 (mass%)
(e)
Zr/Y
10
9
8
7
6
5
4
3
Dredged samples (this study)
Drift pumice (Y22a)
Melt inclusion in Ol/Cpx (Y22a)
Drift pumice from 1986/1992
eruptions (S98)
(f)
La/Sm
10
9
8
7
6
5
4
3
45
50
55
60
65
SiO_2 (mass%)
(g)
Sample/N-MORB
1000
100
10
1
This study
Western line
D03R01
D03R03
D08R03
D08R04
D08R11
NE line
D07R01
D07R05
SE line
D06R01
D06R02
Previous study
Drift pumice
(Y22a, Y87)
Cs Ba U Ta Ce Pr Nd Hf Eu Tb Ho Er Yb
Rb Th Nb La Pb Sr Zr Sm Gd Dy Y Tm Lu

Fig. 4

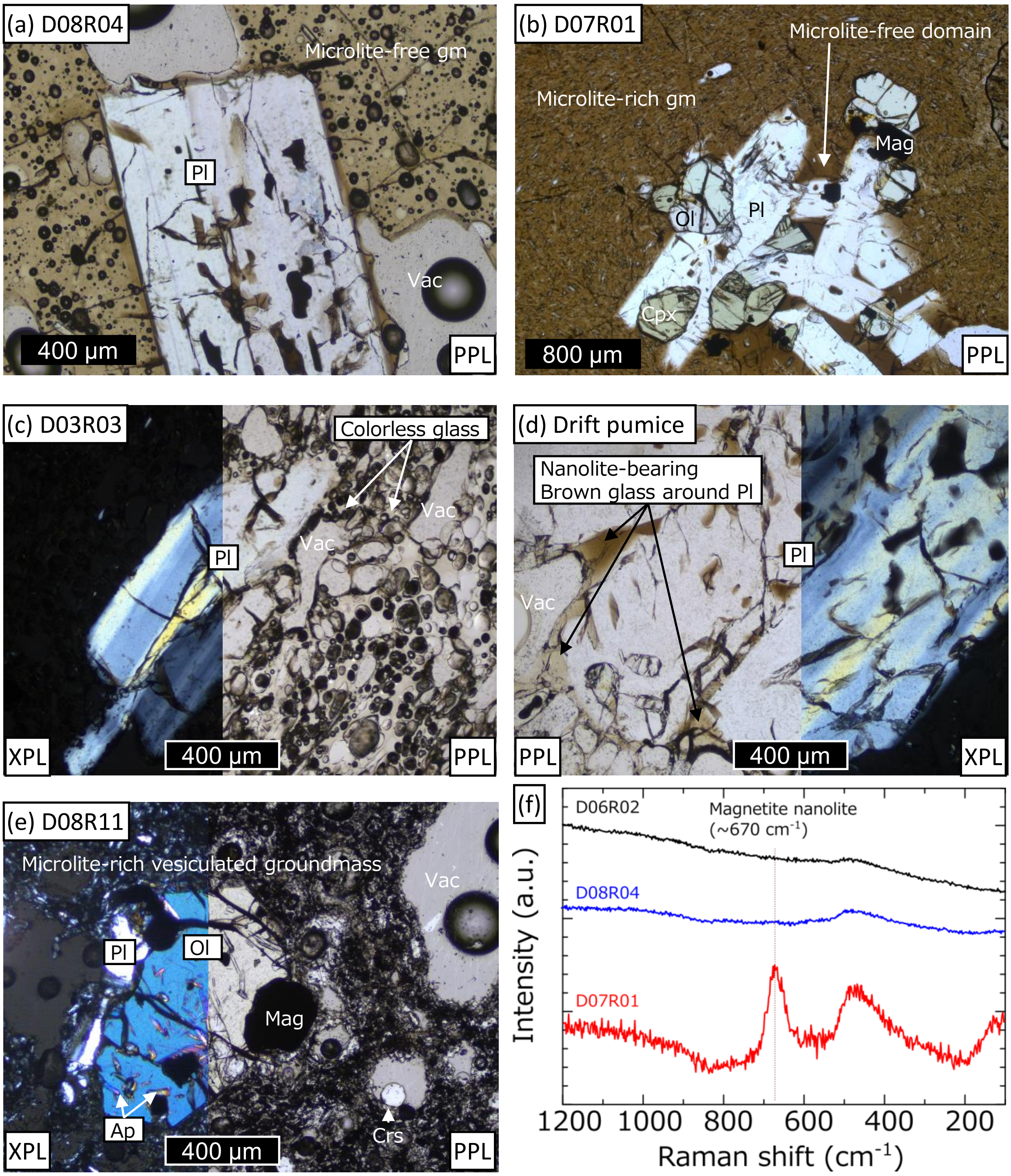

(a) D08R04
Microlite-free gm
Pl
Vac
400 μm
PPL
(b) D07R01
Microlite-free domain
Microlite-rich gm
Mag
Ol
Pl
Cpx
800 μm
PPL
(c) D03R03
Colorless glass
Vac
Vac
Pl
XPL
400 μm
PPL
(d) Drift pumice
Nanolite-bearing
Brown glass around Pl
Pl
Vac
PPL
400 μm
XPL
(e) D08R11
Microlite-rich vesiculated groundmass
Vac
Pl
Ol
Mag
Ap
Crs
XPL
400 μm
PPL
(f)
D06R02
Magnetite nanolite
(~670 cm^{-1})
D08R04
D07R01
Intensity (a.u.)
1200
1000
800
600
400
200
Raman shift (cm^{-1})

Fig. 5

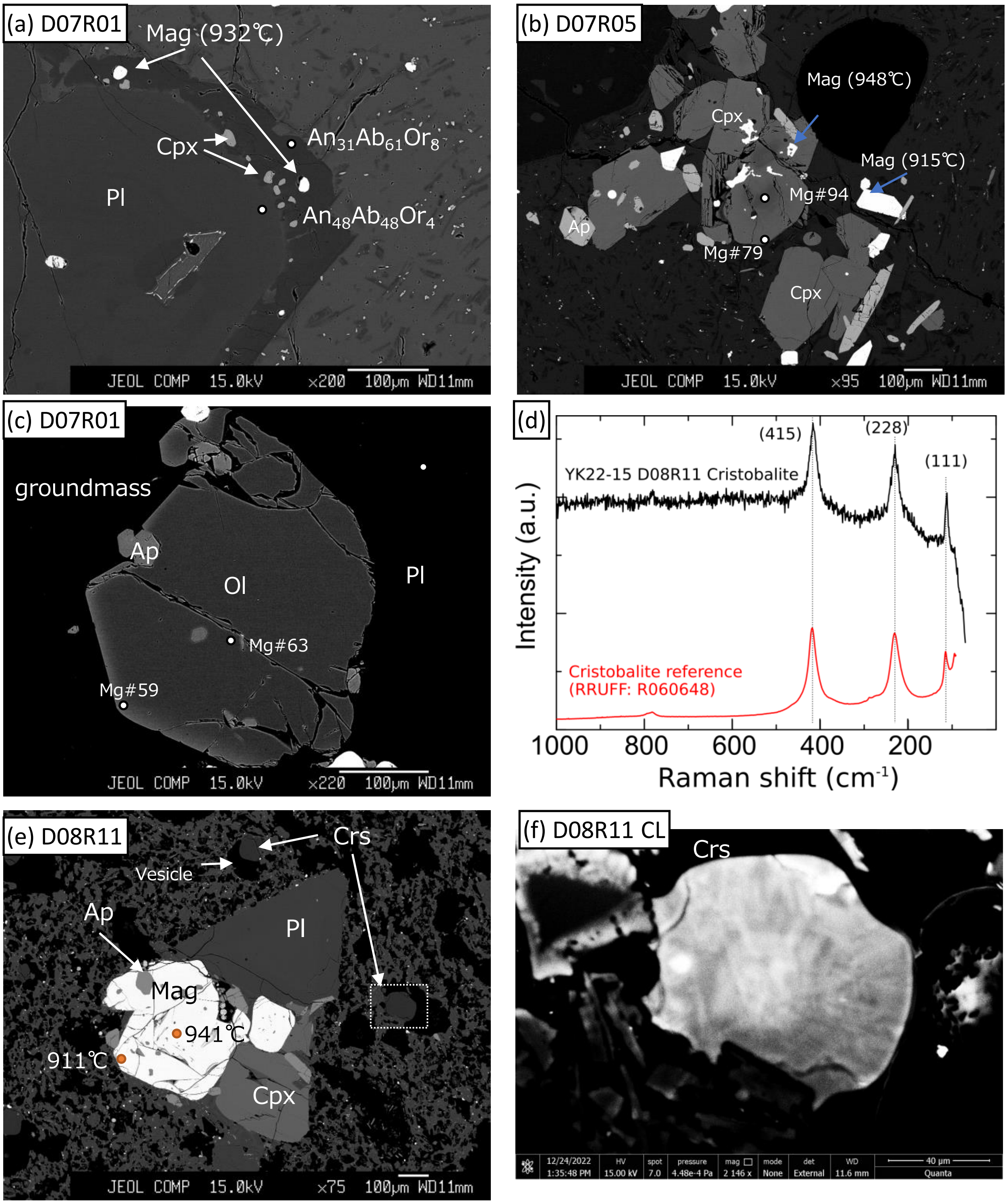
(a) D07R01
Mag (932℃)
Cpx
$An_{31}Ab_{61}Or_8$
Pl
$An_{48}Ab_{48}Or_4$
JEOL COMP 15.0kV ×200 100μm WD11mm
(b) D07R05
Mag (948℃)
Cpx
Mag (915℃)
Mg#94
Ap
Mg#79
Cpx
JEOL COMP 15.0kV ×95 100μm WD11mm
(c) D07R01
groundmass
Ap
Ol
Pl
Mg#63
Mg#59
JEOL COMP 15.0kV ×220 100μm WD11mm
(d)
(415)
(228)
(111)
YK22-15 D08R11 Cristobalite
Intensity (a.u.)
Cristobalite reference
(RRUFF: R060648)
1000
800
600
400
200
Raman shift (cm^{-1})
(e) D08R11
Crs
Vesicle
Ap
Pl
Mag
941℃
911℃
Cpx
JEOL COMP 15.0kV ×75 100μm WD11mm
(f) D08R11 CL
Crs
12/24/2022 1:35:48 PM
HV 15.00 kV
spot 7.0
pressure 4.48e-4 Pa
mag 2 146 x
mode None
det External
WD 11.6 mm
40 μm
Quanta

Fig. 6

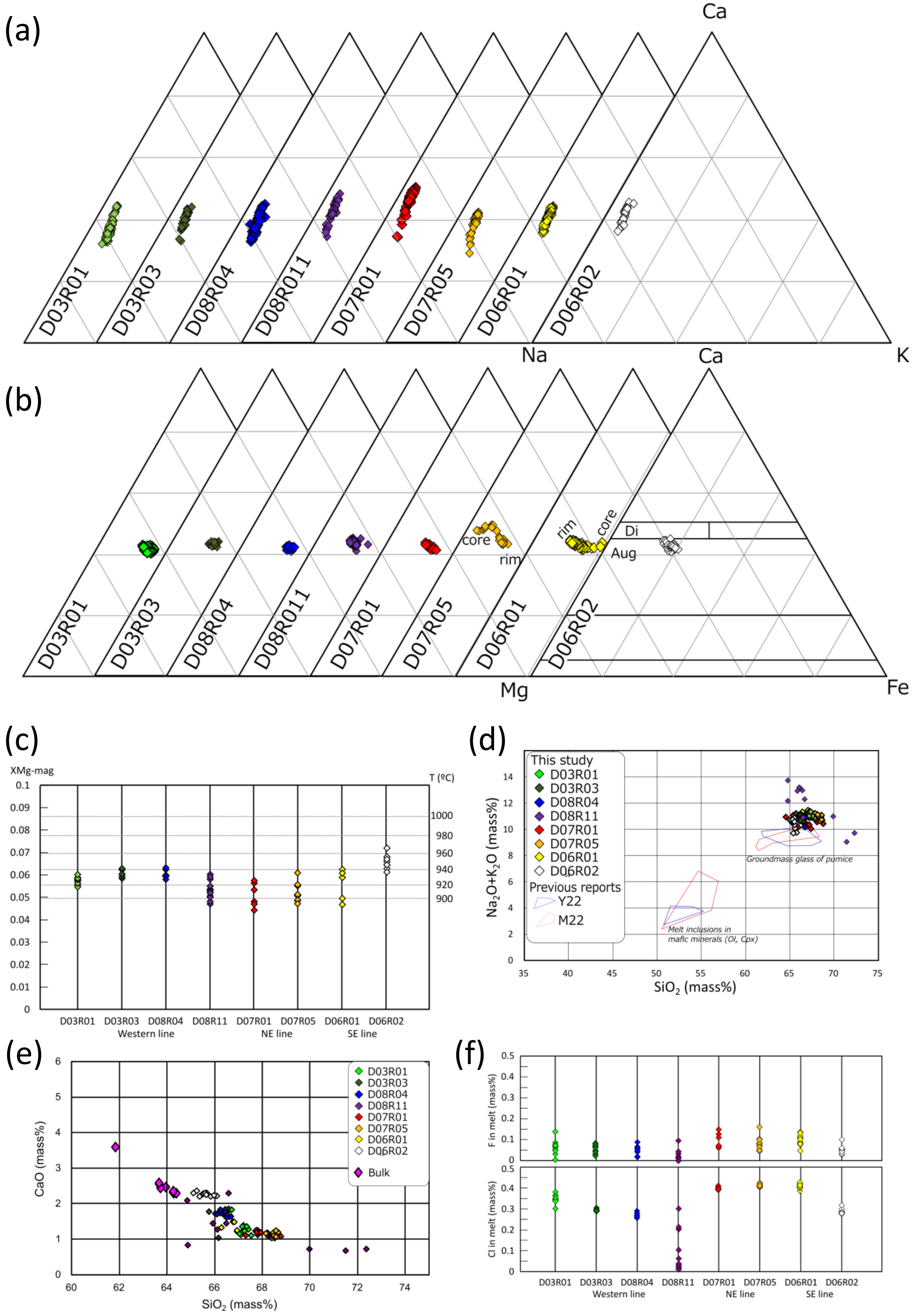
(a)
Ca
D03R01
D03R03
D08R04
D08R011
D07R01
D07R05
D06R01
D06R02
Na
K
(b)
Ca
core
rim
rim
core
Di
Aug
D03R01
D03R03
D08R04
D08R011
D07R01
D07R05
D06R01
D06R02
Mg
Fe
(c)
XMg-mag
0.1
0.09
0.08
0.07
0.06
0.05
0.04
0.03
0.02
0.01
0
T (ºC)
1000
980
960
940
920
900
D03R01
D03R03
D08R04
D08R11
D07R01
D07R05
D06R01
D06R02
Western line
NE line
SE line
(d)
This study
D03R01
D03R03
D08R04
D08R11
D07R01
D07R05
D06R01
D06R02
Previous reports
Y22
M22
Groundmass glass of pumice
Melt inclusions in mafic minerals (Ol, Cpx)
Na_2O+K_2O (mass%)
14
12
10
8
6
4
2
0
35
40
45
50
55
60
65
70
75
SiO_2 (mass%)
(e)
6
5
4
3
2
1
0
CaO (mass%)
60
62
64
66
68
70
72
74
SiO_2 (mass%)
D03R01
D03R03
D08R04
D08R11
D07R01
D07R05
D06R01
D06R02
Bulk
(f)
0.5
0.4
0.3
0.2
0.1
0
F in melt (mass%)
0.5
0.4
0.3
0.2
0.1
0
Cl in melt (mass%)
D03R01
D03R03
D08R04
D08R11
D07R01
D07R05
D06R01
D06R02
Western line
NE line
SE line

Fig. 7

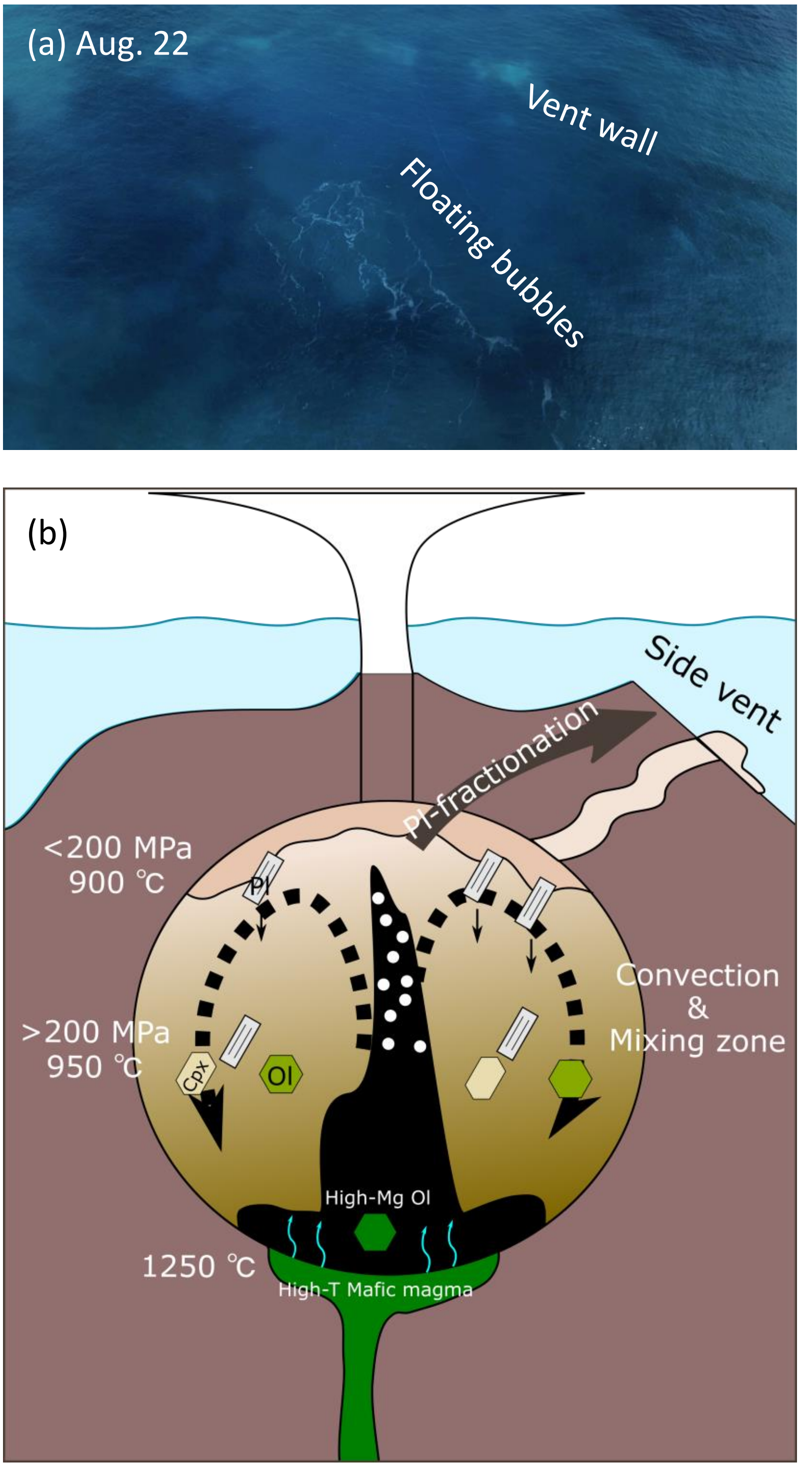
(a) Aug. 22
Vent wall
Floating bubbles
(b)
Side vent
Pl-fractionation
<200 MPa
900 ℃
Pl
Convection
&
Mixing zone
>200 MPa
950 ℃
Cpx
Ol
High-Mg Ol
1250 ℃
High-T Mafic magma

	Western line							
Sample No.	D03R01	D03R02	D03R03	D03R04	D04R01	D08R03	D08R04	D08R11
type	lapilli	pumice	pumice	pumice	pumice	lapilli	lapilli	pumice
microlite	rich	-	free	-	-	-	free	rich
in mass%								
SiO_2	63.06	61.33	62.74	61.04	60.43	62.52	62.47	63.02
TiO_2	0.57	0.59	0.58	0.59	0.65	0.59	0.58	0.57
Al_2O_3	16.57	16.43	16.56	16.17	16.74	16.39	16.66	16.51
Fe_2O_3	4.68	5.30	4.74	5.46	6.03	5.17	4.91	4.60
MnO	0.17	0.17	0.17	0.17	0.19	0.17	0.17	0.17
MgO	0.85	1.50	1.02	1.86	1.42	1.04	1.01	0.94
CaO	2.26	3.15	2.42	3.59	3.36	2.40	2.54	2.31
Na_2O	5.04	4.94	5.06	4.76	4.82	4.91	4.95	5.05
K_2O	5.11	4.65	5.02	4.63	4.56	5.14	5.04	5.09
P_2O_5	0.22	0.24	0.23	0.23	0.28	0.24	0.24	0.22
Total	98.52	98.30	98.53	98.48	98.48	98.57	98.57	98.47
LOI	0.82	1.25	1.60	1.47	1.87	0.44	0.47	1.75
in ppm								
Sc	5.765		4.607			3.48	5.078	2.703
Co	5.105		5.44			5.911	6.039	5.104
Ni	0.604		0.85			0.69	0.573	0.532
Cu	15.668		13.926			17.532	23.696	12.898
Rb	102.895		97.786			101.468	97.946	97.351
Sr	381.091		401.854			385.298	432.896	380.95
Y	31.473		30.462			31.749	30.999	30.792
Zr	282.1		266.22			278.422	268.842	255.013
Nb	11.603		11.139			11.44	11.039	11.041
Cs	2.044		1.963			2.018	1.939	1.944
Ba	1628.653		1557.937			1567.935	1571.212	1560.552
La	80.889		77.939			81.187	79.134	78.154
Ce	151.691		145.449			151.712	148.648	146.606
Pr	16.309		15.722			16.416	16.095	15.904
Nd	58.724		56.303			59.309	57.961	57.213
Sm	9.68		9.476			9.809	9.673	9.545
Eu	1.953		1.909			1.982	1.991	1.961

Gd	7.058	6.818	7.292	7.028	6.928
Tb	1.086	1.047	1.098	1.061	1.061
Dy	5.753	5.632	5.912	5.698	5.698
Ho	1.165	1.122	1.179	1.155	1.153
Er	3.585	3.522	3.654	3.602	3.601
Tm	0.539	0.513	0.541	0.517	0.525
Yb	3.684	3.554	3.724	3.594	3.586
Lu	0.568	0.549	0.575	0.557	0.554
Hf	6.868	6.538	6.959	6.678	6.531
Ta	0.525	0.512	0.533	0.515	0.513
Tl	0.237	0.262	0.232	0.22	0.079
Pb	17.641	17.386	17.578	17.279	12.601
Th	21.248	20.221	21.474	20.853	20.767
U	6.108	5.829	6.219	5.97	6.169

NE line			SE line	
D07R01	D07R05	D07R09	D06R01	D06R02
lava	lava	woody pumice	lapilli	lapilli
rich	rich	-	rich	free
63.13	63.27	62.33	62.58	60.70
0.55	0.55	0.55	0.59	0.60
16.47	16.46	16.74	16.50	16.70
4.77	4.67	4.67	5.07	5.85
0.16	0.16	0.16	0.16	0.17
0.95	0.94	1.04	1.04	1.62
2.28	2.26	2.68	2.51	3.53
4.84	4.83	4.90	4.92	4.68
5.31	5.35	5.05	5.13	4.58
0.20	0.20	0.21	0.24	0.26
98.67	98.68	98.34	98.73	98.69
1.03	1.02	2.70	0.63	0.69
3.765	3.171		5.942	5.946
5.951	5.678		6.242	9.864
1.315	1.284		0.745	4.824
22.445	19.442		20.727	34.807
107.589	107.074		103.452	89.679
335.262	340.913		393.279	500.262
31.204	31.177		31.28	29.066
290.57	290.074		284.739	244.3
12.01	12.086		11.762	10.175
2.121	2.108		2.039	1.788
1557.2	1558.452		1584.703	1451.749
81.591	81.026		82.04	75.035
152.237	153.946		154.28	139.477
16.384	16.261		16.438	15.138
58.124	58.206		59.568	55.082
9.644	9.598		9.741	9.201
1.839	1.836		1.947	1.963

6.924	6.942	7.104	6.716
1.067	1.065	1.065	1.017
5.753	5.676	5.743	5.456
1.151	1.151	1.16	1.076
3.641	3.673	3.64	3.37
0.531	0.538	0.531	0.488
3.661	3.704	3.618	3.352
0.576	0.574	0.569	0.523
7.19	7.238	6.956	6.081
0.559	0.552	0.542	0.467
0.279	0.287	0.22	0.212
18.213	18.305	17.404	15.525
22.493	22.578	21.507	18.934
6.494	6.522	6.284	5.538

Sample N	D03R01		D03R03		D08R04		D08R11	
Note	core	rim	core	rim	core	rim	core	rim
SiO_2	56.75	59.50	58.32	59.68	57.83	59.62	56.30	60.19
TiO_2	0.01	0.07	0.07	0.06	0.00	0.02	0.06	0.00
Al_2O_3	26.37	24.83	26.23	24.52	25.58	24.54	26.79	24.25
Cr_2O_3	0.00	0.13	0.00	0.01	0.01	0.00	0.04	0.00
FeO*	0.56	0.61	0.49	0.55	0.48	0.42	0.55	0.54
MnO	0.00	0.00	0.02	0.00	0.02	0.00	0.01	0.08
MgO	0.05	0.05	0.06	0.03	0.03	0.07	0.02	0.02
CaO	8.96	7.23	8.82	7.01	8.58	6.89	10.03	7.08
Na_2O	5.82	6.72	6.17	6.97	6.14	6.78	5.59	6.74
K_2O	0.69	0.97	0.79	1.11	0.75	1.00	0.59	1.17
total								
O	8	8	8	8	8	8	8	8
Si	2.57	2.66	2.60	2.68	2.61	2.68	2.54	2.70
Ti	0.00	0.00	0.00	0.00	0.00	0.00	0.00	0.00
Al	1.41	1.31	1.38	1.30	1.36	1.30	1.43	1.28
Cr	0.00	0.00	0.00	0.00	0.00	0.00	0.00	0.00
Fe	0.02	0.02	0.02	0.02	0.02	0.02	0.02	0.02
Mn	0.00	0.00	0.00	0.00	0.00	0.00	0.00	0.00
Mg	0.00	0.00	0.00	0.00	0.00	0.00	0.00	0.00
Ca	0.44	0.35	0.42	0.34	0.42	0.33	0.49	0.34
Na	0.51	0.58	0.53	0.61	0.54	0.59	0.49	0.59
K	0.04	0.06	0.04	0.06	0.04	0.06	0.03	0.07
An	44	35	42	33	42	34	48	34
Ab	52	59	53	60	54	60	49	59
Or	4	6	4	6	4	6	3	7

D07R01		D07R05		D06R01		D06R02	
core	rim	core	rim	core	rim	core	rim
56.48	60.24	58.32	60.40	57.86	57.99	56.52	58.64
0.05	0.08	0.04	0.04	0.00	0.07	0.06	0.04
26.72	24.32	25.45	24.48	26.40	25.11	25.85	24.31
0.05	0.00	0.00	0.00	0.00	0.00	0.03	0.04
0.58	0.60	0.48	0.45	0.48	0.48	0.70	0.62
0.00	0.05	0.04	0.00	0.01	0.09	0.05	0.00
0.04	0.06	0.06	0.01	0.08	0.04	0.02	0.04
9.88	6.33	8.20	6.64	9.09	7.92	9.47	7.52
5.47	6.88	6.35	7.11	5.95	6.56	6.06	6.69
0.53	1.25	0.88	1.35	0.81	0.92	0.78	1.02
8	8	8	8	8	8	8	8
2.55	2.70	2.63	2.69	2.59	2.63	2.56	2.66
0.00	0.00	0.00	0.00	0.00	0.00	0.00	0.00
1.42	1.28	1.35	1.29	1.39	1.34	1.38	1.30
0.00	0.00	0.00	0.00	0.00	0.00	0.00	0.00
0.02	0.02	0.02	0.02	0.02	0.02	0.03	0.02
0.00	0.00	0.00	0.00	0.00	0.00	0.00	0.00
0.00	0.00	0.00	0.00	0.01	0.00	0.00	0.00
0.48	0.30	0.40	0.32	0.44	0.38	0.46	0.37
0.48	0.60	0.55	0.61	0.52	0.58	0.53	0.59
0.03	0.07	0.05	0.08	0.05	0.05	0.05	0.06
48	31	40	31	44	38	44	36
48	61	55	61	52	57	51	58
3	7	5	8	5	5	4	6

Sample No.	D03R01	D03R03	D08R04	D08R11	D07R01	D07R05	
Note						core	rim
SiO_2	52.66	52.58	52.65	52.65	52.42	53.39	53.00
TiO_2	0.38	0.39	0.36	0.34	0.40	0.19	0.38
Al_2O_3	0.64	1.48	0.67	1.82	0.85	1.68	1.22
Cr_2O_3	0.02	0.10	0.00	0.00	0.05	0.09	0.07
FeO*	9.43	9.09	9.61	8.79	9.10	4.13	9.62
MnO	0.19	0.99	0.11	0.68	0.13	0.12	0.79
MgO	15.36	15.35	15.21	15.44	15.45	17.50	15.26
CaO	19.88	20.22	20.16	20.53	20.19	23.32	20.59
Na_2O	0.45	0.38	0.48	0.38	0.41	0.22	0.45
K_2O	0.01	0.01	0.00	0.00	0.00	0.00	0.00
total	99.03	100.59	99.23	100.63	99.00	100.63	101.37
O	6	6	6	6	6	6	6
Si	1.97	1.94	1.97	1.94	1.96	1.93	1.94
Ti	0.01	0.01	0.01	0.01	0.01	0.01	0.01
Al	0.03	0.06	0.03	0.08	0.04	0.07	0.05
Cr	0.00	0.00	0.00	0.00	0.00	0.00	0.00
Fe^{3+}	0.04	0.06	0.05	0.06	0.05	0.07	0.07
Fe^{2+}	0.25	0.22	0.25	0.21	0.24	0.06	0.22
Mn	0.01	0.03	0.00	0.02	0.00	0.00	0.02
Mg	0.86	0.84	0.85	0.85	0.86	0.94	0.83
Ca	0.80	0.80	0.81	0.81	0.81	0.90	0.81
Na	0.03	0.03	0.03	0.03	0.03	0.02	0.03
K	0.00	0.00	0.00	0.00	0.00	0.00	0.00
Mg#	77	79	77	80	78	94	79
P (MPa, P20) †	388	261	254	236	177	445	276

D06R01		D06R02		D03R01	D03R03	D08R04	D07R01
core	rim						core
53.42	52.62	52.85	SiO_2	37.41	37.12	37.64	36.44
0.18	0.41	0.39	TiO_2	0.05	0.02	0.00	0.02
0.93	1.69	1.33	Al_2O_3	0.00	0.01	0.02	0.00
0.02	0.00	0.02	Cr_2O_3	0.00	0.01	0.00	0.00
11.45	8.87	9.78	FeO*	31.03	30.51	30.31	32.50
1.07	0.65	0.69	MnO	1.57	1.54	1.52	1.68
14.19	15.05	15.11	MgO	31.64	32.53	32.09	30.49
19.88	20.58	20.12	CaO	0.15	0.17	0.18	0.15
0.46	0.43	0.38	Na_2O	0.03	0.00	0.01	0.01
0.00	0.03	0.02	K_2O	0.00	0.00	0.01	0.01
101.59	100.33	100.69	NiO	0	0	0	0
			total	101.88	101.91	101.77	101.30
6	6	6	O	4	4	4	4
1.97	1.94	1.95	Si	1.00	0.99	1.00	0.99
0.00	0.01	0.01	Ti	0.00	0.00	0.00	0.00
0.04	0.07	0.06	Al	0.00	0.00	0.00	0.00
0.00	0.00	0.00	Cr	0.00	0.00	0.00	0.00
0.04	0.05	0.05	Fe	0.69	0.68	0.68	0.74
0.31	0.23	0.26	Mn	0.04	0.03	0.03	0.04
0.03	0.02	0.02	Mg	1.26	1.29	1.28	1.24
0.78	0.83	0.83	Ca	0.00	0.00	0.01	0.00
0.79	0.81	0.80	Na	0.00	0.00	0.00	0.00
0.03	0.03	0.03	K	0.00	0.00	0.00	0.00
0.00	0.00	0.00					
72	78	76		64	66	65	63
371	279	215					

	R07R05		D06R01	D06R02
rim	core	rim		
36.36	36.51	37.15	37.10	37.38
0.00	0.01	0.01	0.00	0.00
0.02	0.01	0.69	0.01	0.02
0.00	0.00	0.02	0.00	0.01
34.63	32.52	35.46	31.03	29.18
1.72	1.65	1.79	1.41	1.23
28.87	30.20	26.52	31.94	33.40
0.15	0.15	0.19	0.16	0.17
0.01	0.04	0.18	0.00	0.01
0.02	0.00	0.16	0.02	0.00
0.001	0	0	0	0.002
101.77	101.09	102.17	101.67	101.39
4	4	4	4	4
0.99	0.99	1.01	0.99	1.00
0.00	0.00	0.00	0.00	0.00
0.00	0.00	0.02	0.00	0.00
0.00	0.00	0.00	0.00	0.00
0.79	0.74	0.81	0.70	0.65
0.04	0.04	0.04	0.03	0.03
1.18	1.23	1.08	1.28	1.33
0.00	0.00	0.01	0.00	0.00
0.00	0.00	0.01	0.00	0.00
0.00	0.00	0.01	0.00	0.00
60	62	57	65	67

Sample No.	D03R01	D03R03	D08R04	D08R11		D07R01	
Note				in Cpx anc	gm	in Pl rim	gm
SiO_2	0.10	0.09	0.08	0.09	0.10	0.16	0.13
TiO_2	10.93	10.53	10.38	11.26	10.95	11.27	12.26
Al_2O_3	2.81	2.83	2.95	2.61	2.70	2.59	2.07
Cr_2O_3	0.06	0.00	0.02	0.12	0.00	0.09	0.13
FeO*	78.09	77.56	78.01	77.77	78.35	75.66	75.54
MnO	1.05	0.96	1.02	0.94	1.12	0.17	1.10
MgO	2.81	2.70	2.91	2.68	2.17	2.58	2.08
CaO	0.03	0.00	0.03	0.03	0.01	0.11	0.03
Na_2O	0.01	0.00	0.03	0.00	0.05	0.00	0.00
K_2O	0.04	0.01	0.00	0.02	0.00	0.01	0.10
total	95.92	94.68	95.44	95.52	95.45	92.64	93.44
O	4	4	4	4	4	4	4
Si	0.00	0.00	0.00	0.00	0.00	0.01	0.00
Ti	0.29	0.28	0.28	0.30	0.29	0.31	0.34
Al	0.12	0.12	0.12	0.11	0.11	0.11	0.09
Cr	0.00	0.00	0.00	0.00	0.00	0.00	0.00
Fe^{3+}	1.49	1.50	1.50	1.48	1.49	1.46	1.45
Fe^{2+}	0.82	0.83	0.82	0.83	0.85	0.85	0.85
Mn	0.03	0.03	0.03	0.03	0.03	0.01	0.03
Mg	0.15	0.14	0.15	0.14	0.12	0.14	0.11
Ca	0.00	0.00	0.00	0.00	0.00	0.00	0.00
Na	0.00	0.00	0.00	0.00	0.00	0.00	0.00
K	0.00	0.00	0.00	0.00	0.00	0.00	0.00
XMg-mag †	0.060	0.058	0.062	0.058	0.047	0.057	0.047
T_XMg (° C) ‡	934	929	940	928	893	926	892

D07R05	D06R01		D06R02	D08R11
	core	rim		Crs
0.09	0.08	0.07	0.10	98.21
11.90	10.49	10.22	9.33	0.143
2.59	2.99	2.87	3.19	0.973
0.06	0.05	0.06	0.05	0.02
77.23	78.10	78.43	77.51	0.066
1.14	0.85	0.94	0.84	0.037
2.32	2.93	2.31	3.12	0.006
0.01	0.00	0.00	0.00	0.014
0.00	0.02	0.05	0.00	0.597
0.01	0.02	0.04	0.00	0.005
95.34	95.52	94.99	94.14	
4	4	4	4	2
0.00	0.00	0.00	0.00	0.99
0.32	0.28	0.28	0.25	0.00
0.11	0.12	0.12	0.13	0.0115
0.00	0.00	0.00	0.00	0.00
1.46	1.50	1.50	1.52	0.00
0.84	0.82	0.85	0.81	0.00
0.03	0.03	0.03	0.03	0.00
0.12	0.15	0.12	0.17	0.00
0.00	0.00	0.00	0.00	0.00
0.00	0.00	0.00	0.00	0.0116
0.00	0.00	0.00	0.00	0.00
0.051	0.063	0.050	0.067	
905	941	902	953	

Yoshida et al. The nature of the proximal volcaniclastic materials from the 2021 eruption Fukutoku-Oka-no-Ba in the Izu-Bonin arc

Supplementary Material 1

Dredge assembly used during the cruise YK22-15

During the cruise YK22-15, we used a Satsuki type dredger and depressor-towing body. This assembly is employed to protect the opto-electrical composite cable from any damaging during dredging (Fig. S1). The Satsuki type dredger was connected to the depressor-towing body by a lead wire with 200 m length. The position of the dredger was monitored by a transponder attached to the depressor-towing body (Fig. S2a). The Satsuki type dredger has a size of 800 mm × 740 mm × 120 mm (width, height, and length, respectively) and ~240 kg.

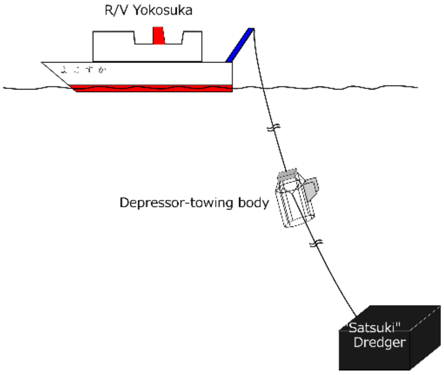

Fig. S1. Schematic image of the dredge assembly.

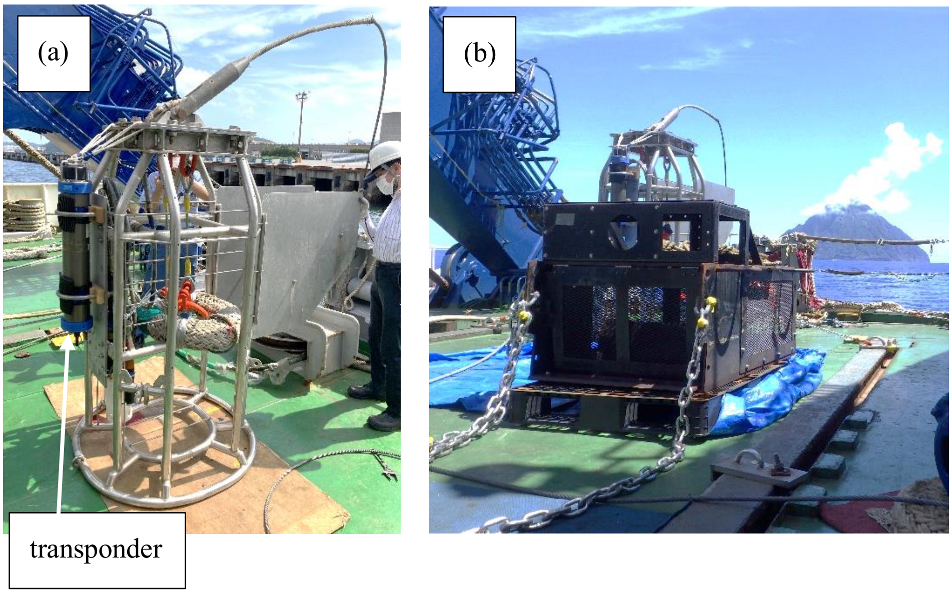

Figure S2. (a) A depressor-towing body equipped with a transponder. (b) Photograph of Satsuki type dredger which is ready for operation.

Table S1. Details of the dredge positions

Dredge number	Hit bottom		Off bottom		Depth (m)[*1]		Tension max. (kN)	Survey time (hh:mm)
	Lat.（SOQ[*1]）	Lon.（SOQ[*1]）	Lat.（SOQ[*1]）	Lon.（SOQ[*1]）	On the bottom	Off the Bottom		
D03	24-16.8737N	141-25.6601E	24-16.8458N	141-25.8852E	446	353	41.6	0:36
D04	24-22.0755N	141-26.4721E	24-22.5723N	141-26.4072E	324	299	13.0	0:59
D05	24-18.5790N	141-26.2145E	24-18.6416N	141-26.6848E	369	182	18.1	1:00
D06	24-14.6284N	141-31.1048E	24-15.1767N	141-30.6928E	649	361	16.6	1:12
D07	24-20.6611N	141-31.6256E	24-20.3546N	141-31.0876E	525	256	28.1	1:17
D08	24-16.8088N	141-26.0734E	24-16.6746N	141-26.5212E	383	294	17.3	1:02

*SOQ = SGK Transponder's position

*SOJ = Ship's position

Table S2. Trace element analysis of secondary standard (JB-2) and the reference value

Sample	JB-2, mea	JB-2, reference* (μg/g)
Sc	51.728	54.08
Co	34.64	37.57
Ni	12.417	14.77
Cu	209.443	222.1
Rb	5.732	6.4
Sr	175.628	178.2
Y	21.115	23.56
Zr	43.894	48.25
Nb	0.439	0.565
Cs	0.754	0.8
Ba	208.065	218.1
La	2.131	2.281
Ce	6.297	6.552
Pr	1.096	1.129
Nd	6.168	6.392
Sm	2.208	2.266
Eu	0.792	0.836
Gd	3.15	3.123
Tb	0.572	0.5863
Dy	3.915	3.868
Ho	0.854	0.863
Er	2.584	2.537
Tm	0.376	0.393
Yb	2.525	2.529
Lu	0.382	0.3894
Hf	1.49	1.487
Ta	0.032	0.0396
Tl	0.036	0.034
Pb	4.963	5.25
Th	0.252	0.2576
U	0.155	0.1528

*Reference of JB-2 is taken from GeoReM database
(Jochum et al. Geostand. Geoanal. Res. 40, 333-350, 2016)